Effects of Heat Transfer Coefficient Variation on Nuclear Thermal Propulsion Engine Performance

Daria Nikitaeva[1], Corey D. Smith[1], Matthew Duchek[2]

[1]Advanced Projects Huntsville, Analytical Mechanics Associates, Huntsville, AL, 35806
[2]Advanced Projects Denver, Analytical Mechanics Associates, Denver, CO, 80211

Primary Author Contact Information: 702-287-6852, daria.d.nikitaeva@ama-inc.com

A physics-based Nuclear Thermal Propulsion (NTP) Testing Reference Design (TRD) power balance model was coded in Simulink to investigate engine performance for various design and parameter modifications. Since the primary mode of heat transfer in NTP engines is convective, the convective heat transfer coefficient (HTC) is a key parameter that requires accurate representation. The industry standard Westinghouse correlation has an uncertainty of ±20% which was investigated in this study. The results showed that a 20% decrease in the HTC led to a 4.14% increase in maximum fuel temperature while a 20% decrease in the HTC led to a 1.81% decrease in maximum fuel temperature suggesting that narrowing the uncertainty of this correlation through experimental work would be a critical step in the development of NTP engines. Furthermore, a maximum fuel temperature relationship with specific impulse was developed for the TRD engine which showed potential engine operation between specific impulse values of 715 and 900 seconds with minimal changes to the engine design. This graph could be useful for high level vehicle performance estimations for fuel types with different maximum operating temperatures.

I. INTRODUCTION

Nuclear Thermal Propulsion (NTP) is an in-space propulsion method which underwent significant development in the United States from 1950s through the early 1970s during the Project Rover and Nuclear Engine for Rocket Vehicle Application (NERVA) programs. The goal of these two programs was to create a propulsion system capable of transporting humans to Mars and provide a reusable lunar shuttle. Unlike chemical propulsion, NTP does not depend on combustion of an oxidizer and fuel to produce thrust; instead, a propellant is pumped into a nuclear reactor and heated to high temperatures before being expelled through a nozzle. Essentially, the NTP-based engine is a monopropellant system[1]. In the early 1970s, the NERVA program was cancelled in part because the Cold War was ending, the United States made successful crewed landings on the Moon, and there was less interested in large funding to Mars as well as other political factors. Many studies and some development programs have been completed since

this program, but none have reached the development status demonstrated in Rover/NERVA. In recent years, there has been renewed interest in development of NTP systems for crewed space exploration. Therefore, government, academia, and industry have been developing modern hardware and modeling approaches to bolster NTP development. These developments have allowed quick performance estimates to be made to provide insight into the expected system performance given a change to selected parameters. One of these analyses is presented in this paper which investigates how varying the heat transfer coefficient within its error bounds affects the NTP engine performance and the propellant state points according to the flow schedule throughout the engine.

The NTP Testing Reference Design (TRD)[2] schematic, as seen in Fig. 1, shows the expander cycle NTP engine using hydrogen as the sole propellant. The hydrogen flow starts out by exiting the propellant tank when the pump shut-off valve (PSOV) is opened and enters the boost pump at State 1. The boost pump is needed to prevent cavitation from occurring at the inlet to the main pumps. A boost pump was not needed in the NERVA program since those were bleed cycles which did not require as high of a system pressure as the expander cycle.

The flow exits the boost pump and enters the main pumps at State 2 from which it exits at State 3 to go through the pump bypass valve (PBV). From the PBV, the flow exits at State 4 and is split between the moderator element control valve (MECV) and the REGenerative cooling Control Valve (REGCV). From the exit of the REGCV at State 6, the flow provides regenerative cooling to the nozzle and exits at State 7 into the control drum/reflector channels to also provide cooling and exits at State 8. From the exit of the MECV at State 10, the flow enters the moderator block cooling channels and exits at State 11. The exit flows from the moderator block and the control drum/reflector region mix at State 12 and the flow is split between the boost turbine at State 13, the main turbines at State 15, and the turbine control valve (TBCV) at State 17. The flows from the boost turbine, main turbines, and TBCV exit at States 14, 16, and 18, respectively and mix at State 19. The TurBine Valve (TBV) is used to provide additional pressure regulation to ensure robust control and

throttlability of the engine by changing the turbine pressure ratio.

The mixed flow at State 19 enters the fuel element control valve (FECV) and exits at State 20 to enter the fuel elements. The flow is superheated and exits at State 21 which corresponds to the chamber conditions. The flow then goes through the converging/diverging nozzle to become accelerated to provide thrust and exits the engine system at State 22.
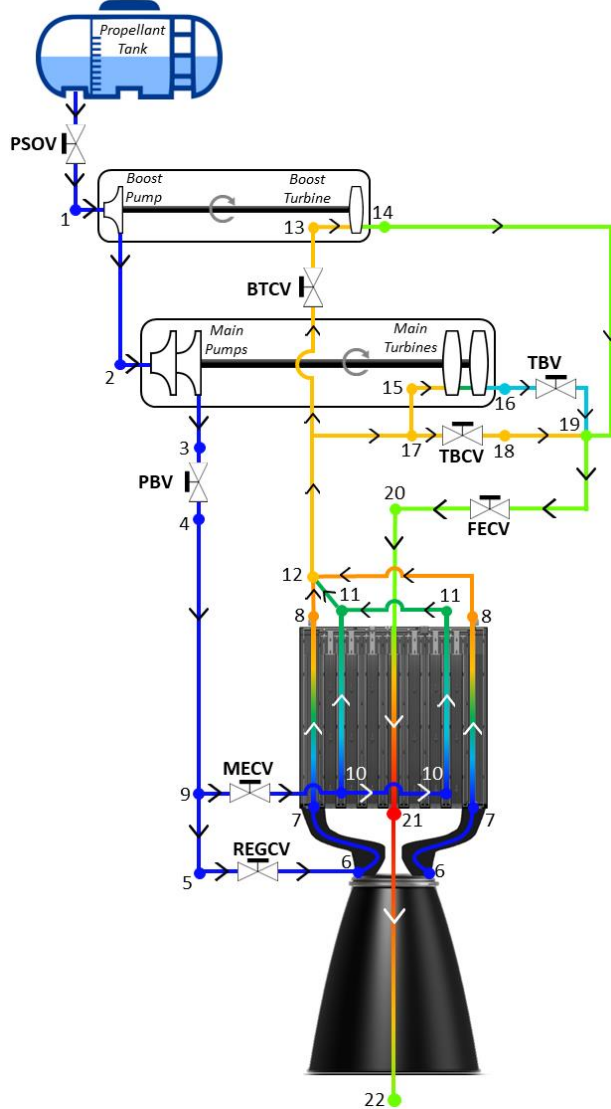

Fig. 1. NTP Testing Reference Design Schematic

II. NTP ENGINE MODEL

The TRD was modeled in Simulink with the physics of each major component coded using physics-based correlations. Previous work[2] has provided an in-depth view of the approach that was used to increase the fidelity of the turbomachinery components using affinity laws and efficiency contour plots. However, it did not outline the modeling approaches to the other components which will be included in this work.

II.A. Turbomachinery

This section provides an overview of the affinity laws used in the model. The pump work $\dot{W}_p$ and rotating velocity ω are shown in Eq. 1 and Eq. 2, respectively which are based on the pump mass flow rate $\dot{m}_p$, fluid density ρ, pressure P, physical pump diameter D_p, and specific speed of the pump n_{s_p}. Eq. 3 describes the specific diameter which can be used to extract the pump efficiency from a contour plot[3].

$$\dot{W}_p = \frac{\dot{m}_p(P_{out} - P_{in})}{\rho} \tag{1}$$

$$\omega = \frac{n_{s_p}(g_0 H_p)^{3/4}}{\sqrt{\dot{\forall}_p}} = \frac{n_{s_p}(P_{out} - P_{in})^{3/4}}{\rho^{1/4}\sqrt{\dot{m}_p}} \tag{2}$$

$$d_{s_p} = \frac{D_p(g_0 H_p)^{1/4}}{\sqrt{\dot{\forall}_p}} = \frac{D_p[\rho(P_{out} - P_{in})]^{1/4}}{\sqrt{\dot{m}_p}} \tag{3}$$

Similarly, the affinity laws for the turbine are expressed through the fluid enthalpy instead of the pressure. The pump dictates the performance that the turbine must provide, therefore the turbine work must equal the pump work $\dot{W}_{turb} = \dot{W}_{pump}$ and the turbine rotational velocity is equal to the pump velocity. Using this, the expression for the required turbine specific speed n_{s_t} and specific diameter d_{s_t} (based on the physical turbine diameter D_t) are shown in Eq. 4 and Eq. 5, respectively.

$$n_{s_t} = \frac{\omega\sqrt{\dot{\forall}_t}}{(g_0 H_t)^{3/4}} = \frac{\omega\sqrt{\dot{m}_t}}{\sqrt{\rho}(h_{in} - h_{out})^{3/4}} \tag{4}$$

$$d_{s_t} = \frac{D_t(g_0 H_t)^{1/4}}{\sqrt{\dot{\forall}_t}} = \frac{D_t\sqrt{\rho}(h_{in} - h_{out})^{1/4}}{\sqrt{\dot{m}_t}} \tag{5}$$

The turbines are throttled by controlling the mass flow rate. Therefore, depending on the turbine specific speed, rotational velocity, and required work that needs to be produced, the mass flow rate can be determined by using a modified and simplified expression of the 1st Law of Thermodynamics for an open system, as shown in Eq. 6. The details of its derivation were provided in previous work[2]. Since the turbine specific speed and specific diameter are known from Eq. 4 and Eq. 5, the turbine efficiency can be found from a contour plot. Using the isentropic efficiency, the isentropic outlet enthalpy can be found by using Eq. 7 and, in conjunction with the inlet entropy, the outlet pressure can be found to determine the turbine pressure ratio via fluid properties look-up table.

$$\dot{m}_t = (W_{shaft} - \dot{Q}_{in})^{3/5}\left(\frac{n_{s_t}\sqrt{\rho}}{\omega}\right)^{4/5} \tag{6}$$

$$\eta_t = \frac{h_{in}-h_{out}}{h_{in}-h_{out_s}} \rightarrow h_{out_s} = h_{in} - \frac{h_{in}-h_{out}}{\eta_t} \qquad (7)$$

II.B. Cooling Channel Flow

The cooling channel flow analysis is based on a nodal model using a first order iterative upwind CFD scheme and determines both the temperature gains and pressure losses of the fluid at each node as shown in the schematic in Fig. 2. Here, the energy coming into node i of length Δx is the fluid enthalpy $\dot{m}h_i$ (not specific enthalpy) as well as the heat allocated to this node δQ_i. It is assumed that all δQ_i goes into the fluid to result in the energy leaving the node of $\dot{m}h_{i+1}$. This leads to a temperature rise of ΔT and a node exit temperature of T_{i+1}. The heat transfer coefficient $\hbar$ for this study is assumed to be the Westinghouse correlation shown in Eq. 8 with an expected error of $\pm 20\%$ and valid for a Reynolds number between 4,000 and 1.5×10^6 (Ref. 4).

The surface temperature of the node T_{s_i} and the exit temperature T_{i+1} are found by solving Eq. 9 and Eq. 10 simultaneously. The pressure drop within the node is found by incorporating both frictional and momentum pressure losses, as shown in Eq. 11. For the frictional pressure losses, the friction factor that is used is that of Churchill for which the expression together with the coefficients A and B are shown in Eq. 12.
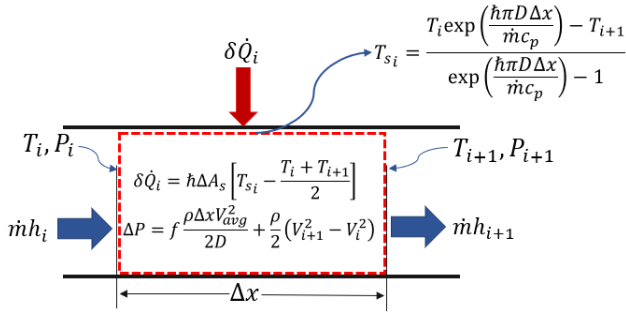

Fig. 2. Reactor Channel Nodal Heat Transfer Schematic

$$\hbar = 0.025 \frac{k}{D} Re^{0.8} Pr^{0.4}\left[1 + 0.3\left(\frac{D}{\sum_{j=1}^{i}\Delta x}\right)^{0.7}\right]\left(\frac{2T_{s_i}}{T_i+T_{i+1}}\right)^{-0.55} \quad (8)$$

$$\delta Q_i = \hbar\Delta A_s\left[T_{s_i} - \frac{T_i+T_{i+1}}{2}\right] \qquad (9)$$

$$T_{s_i} = \frac{T_i exp\left(\frac{\hbar\pi D\Delta x}{\dot{m}c_p}\right)-T_{i+1}}{exp\left(\frac{\hbar\pi D\Delta x}{\dot{m}c_p}\right)-1} \qquad (10)$$

$$\Delta P = f\frac{\rho\Delta x V_{avg}^2}{2D} + \frac{\rho}{2}\left(V_{i+1}^2 - V_i^2\right) \qquad (11)$$

$$f_{CH} = 8\left[\left(\frac{8}{Re}\right)^{12} + \frac{1}{(A+B)^{1.5}}\right]^{1/12}$$

Where: $\qquad (12)$

$$A = \left[2.457\ln\left(\frac{1}{\left(\frac{7}{Re}\right)^{0.9} + 0.27\frac{\varepsilon}{d}}\right)\right]^{16}$$

$$B = \left(\frac{37530}{Re}\right)^{16}$$

The maximum expected average fuel temperature is also of high importance as it determines the performance limitation of the NTP engine. Although angular temperature dependencies will occur in the physical system, their calculation methods will require significant computational effort and will not yield to a practical evaluation of an entire power balance model for the engine. Therefore, the present analysis focuses on an average single channel within the core to simplify the overall analysis. The location of the maximum fuel temperature is calculated by finding the total cross-sectional area of the fuel in the fuel element A_f given the fuel element diameter d_f, the number of channels n, and the channel internal diameter d_{c_i}. This area is divided by n as shown in Eq. 13, thus giving the cross-sectional area of the fuel per channel A_{f_c}. The virtual outer diameter of the channel d_{c_o} is then found by forcing A_{f_c} to equal the outer area around the flow channel as shown in Eq. 14. Although this is not a high-fidelity calculation method, it will still yield results with a small error[4]. The maximum fuel temperature is then calculated by the cylindrical heat transfer expression shown in Eq. 15.

$$A_f = \frac{\pi}{4}\left(d_f^2 - nd_{c_i}^2\right) \rightarrow A_{f_c} = \frac{\pi}{4n}\left(d_f^2 - nd_{c_i}^2\right) \quad (13)$$

$$A_{f_c} = \frac{\pi}{4n}\left(d_f^2 - nd_{c_i}^2\right) = \frac{\pi}{4}\left(d_{c_o}^2 - d_{c_i}^2\right) \rightarrow d_{c_o} = \sqrt{\frac{d_f^2 - nd_{c_i}^2}{n} + d_{c_i}^2} \quad (14)$$

$$T_{f_{max_i}} = \frac{\delta\dot{Q}\ln\left(\frac{d_{c_o}}{d_{c_i}}\right)}{2\pi k_f\Delta x} + T_{s_i} \qquad (15)$$

II.C. Nozzle

The nozzle is the component responsible for converting the potential energy inside the chamber into kinetic energy that is responsible for providing thrust. The calculations for estimating the performance of the nozzle are based on the standard compressible flow relations at location x which are shown in Eq. 16 for the temperature ratio, Eq. 17 for the pressure ratio, Eq. 18 for the maximum mass flow rate, Eq. 19 for the Mach number based on the area ratio, Eq. 20 for the thrust F, and Eq. 21 for the specific impulse I_{sp}.

$$\frac{T_0}{T_e} = 1 + \frac{\gamma-1}{2}M_e^2 \qquad (16)$$

$$\frac{P_0}{P_x} = \left(1 + \frac{\gamma-1}{2} M_x^2\right)^{\frac{\gamma}{\gamma-1}} \qquad (17)$$

$$\dot{m}_{max} = P_0 A^* \sqrt{\frac{\gamma}{RT_0}} \cdot \left(\frac{2}{\gamma+1}\right)^{\frac{\gamma+1}{2(\gamma-1)}} \qquad (18)$$

$$\frac{A^*}{A_x} = M_x \left[\frac{\frac{\gamma+1}{2}}{1+\frac{\gamma-1}{2}M_x^2}\right]^{\frac{\gamma+1}{2(\gamma-1)}} \qquad (19)$$

$$F = \eta_{noz}[\dot{m}v_e + (P_e - P_a)A_e] \qquad (20)$$

$$I_{sp} = \frac{F}{\dot{m}g} \qquad (21)$$

The channels that run inside the nozzle provide forced convective cooling and the same correlations and methods are used to determine the fluid and surface temperatures as were described in the previous section. However, the plume flow uses the Bartz correlation[6] for $\hbar$ as shown in Eq. 19 instead of the Westinghouse correlation. Here, σ is the dimensionless boundary layer factor which is expressed in Eq. 20 where s is the exponent inside the Power-Law Force equation shown in Eq. 21. s is determined by using Eq. 21 alongside a reference state (throat conditions) and a state of interest (at location x).

$$\hbar_x = \frac{0.026}{D_t^{0.2}} \left(\frac{\mu_x^{0.2} c_p}{Pr^{0.6}}\right)_0 \left(\frac{\dot{m}}{A_t}\right)^{0.8} \left(\frac{D_t}{r_c}\right)^{0.1} \left(\frac{A_t}{A_x}\right)^{0.9} \sigma \qquad (22)$$

$$\sigma = \left\{\left[\frac{1}{2}\frac{T_{s_o}}{T_0}\left(1 + \frac{\gamma-1}{2}M_x^2\right) + \frac{1}{2}\right]^{0.8-\frac{s_x}{5}}\left[1 + \frac{\gamma-1}{2}M_x^2\right]^{\frac{s_x}{5}}\right\}^{-1} \qquad (23)$$

$$\mu_x = \mu^* \left(\frac{T_x}{T^*}\right)^{s_x} \qquad (24)$$

II.D. Reactor

To inform the thermal hydraulic modeling discussed in Section II, a comprehensive power distribution of the reactor should be included in the modeling suite. In this work, the radial and axial power profile information is generated using a representative SERPENT input deck that mimics the government TRD. This modeling approach uses probabilistic Monte Carlo methods to estimate the reactor neutronic performance at steady state operation. Key inputs to this tool include the TRD geometry, materials, and power level. The user can also provide interface files that SERPENT will use to axially discretize the temperature and density of selected materials. This addition will allow for temperature-dependent cross-sections and more representative assumptions in the transport solver.

Using the baseline TRD, the primary results of interest include the radial and axial power shape in the fuel, moderator, and reflector through SERPENT's core power distribution (CPD) and material-specific detectors. The CPD flag will generate a high-fidelity power distribution in the fuel lattice, including power per assembly, per channel,

and per axial bin. Each of these results files are post processed in the Simulink suite to have a representative heating profile in all crucial flow channels, as discussed in Section II.B. Iterative feedback is being investigated as a viable option to reach autonomous thermal hydraulic and neutronic convergence.

II.E. Model Assembly

The engine model is assembled in Simulink with each engine component coded separately to provide its operating characteristic and outlet independent of the model itself as shown in Fig. 3. This provides the power to reassemble the engine components easily into alternative cycle configurations without recoding the components.
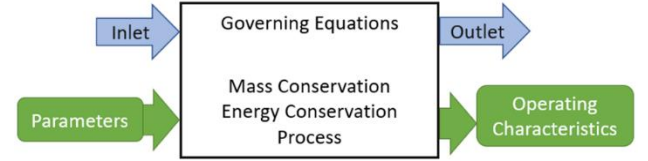

Fig. 3. Arbitrary Engine Component Schematic

For the TRD model configuration, the solution method is shown in Fig. 4. Here, the desired chamber pressure and temperature along with the pump inlet pressure and temperature are set to those of the TRD and are not changed. The guess $\dot{m}$ and $\dot{Q}_{tot}$ are also set to that of the TRD but are iterated as the solution progresses. The fluid flow path is modeled to match that of the TRD shown in Fig. 1. Within the Simulink model, there are two iteration loops that govern the cycle convergence. The internal loop is within the reactor which iterates on $\dot{Q}_{tot}$ to achieve the desired chamber temperature $T_{c_{des}}$. The external loop iterates the reactor inlet pressure to achieve the desired chamber pressure $P_{c_{des}}$ as well as a stable $\dot{m}$ through the nozzle.
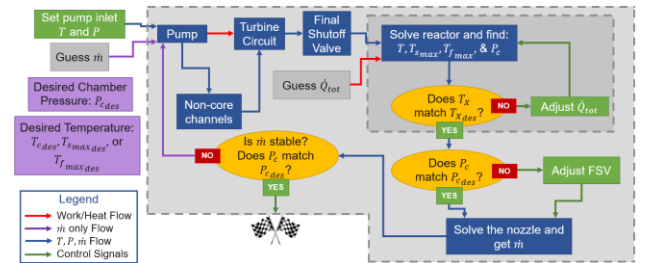

Fig. 4. Solution Flow Diagram

III. ENGINE PERFORMANCE ANALYSIS

The primary purpose of this study is to analyze the performance of the TRD engine by varying the Westinghouse $\hbar$ shown in Eq. 8 by $\pm 20\%$ to capture an expected thermal performance band. This will help determine the impact on the engine performance if the predicted $\hbar$ is not reached. The secondary purpose is to

provide a relationship between the specific impulse I_{sp} and the maximum average fuel temperature for performance estimation when the specific impulse of 900 seconds cannot be reached due to fuel temperature limitations.

The chamber temperature is set to 2700 K to match that of the TRD. Since the system is iterated for both the chamber pressure and temperature to match the desired values, the mass flow rate, specific impulse, and thrust of the engine do not change. There are marginal differences ± 5 K in the temperatures throughout the cycle which contribute to marginal differences in the flow rates through the turbines and TBCV. If the same chamber conditions are achieved, then there would be marginal impact to the overall power balance cycle regardless of the HTC error. However, the same cannot be said for the maximum reactor element temperatures which are summarized in Table I.

Here, it is observed that the HTC plays a critical role in determining the maximum fuel temperature which rises significantly more at an HTC that is 20% lower than the nominal (temperature rise of 127.1 K or 4.14%) than that which is 20% higher than the nominal (temperature drop of 55.5 K or 1.81%). This states that if there is a fuel operational temperature limit within the band of the HTC uncertainty, then there is a possibility of critical reactor failure should the actual HTC be close to the -20% limit. Furthermore, this suggests that experimental investigation of the expected HTC within the fuel element channels is key in maximizing the performance of the TRD engine by decreasing the HTC uncertainty. Both the moderator block and control drum/reflector channels do not exhibit the same high temperature variation as the fuel elements likely due to a much lower overall temperature rise through the channels.

TABLE I. Maximum Reactor Temperatures

Max Fuel Temperature (K)	
HTC ±0%	3065.5
HTC +20%	3010.0
HTC -20%	3192.6
Max Moderator Temperature (K)	
HTC ±0%	575.8
HTC +20%	554.3
HTC -20%	613.1
Max CD/Reflector Temperature (K)	
HTC ±0%	693.4
HTC +20%	669.2
HTC -20%	735.4

This analysis was extended to different chamber temperatures which correspond to different I_{sp} values while the thrust was kept the same by varying the throat diameter. Furthermore, the pump and turbine designs were also modified to accommodate for the increase of $\dot{m}$ as the

I_{sp} is lowered. The resulting maximum fuel temperature versus I_{sp} relationships at the bounding HTC values is shown in Fig. 5. The curves stop at a I_{sp} of 715 seconds which indicate that the TRD design is unable to provide the same amount of thrust below this I_{sp} as the turbine inlet temperature becomes too low and the turbine flow rate becomes too high to retain throttleability of the system through the TBCV. Operating below this I_{sp} will require modifying the component parameters and/or the engine cycle which is outside the scope of this study. The small bumps on these graphs are a product off the accumulation of small errors during convergence, variable fluid properties, and small differences in turbomachinery design convergence with the different operating conditions.
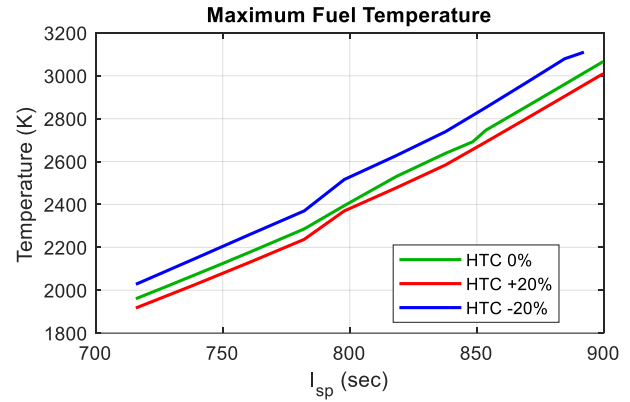

Fig. 5. Maximum Fuel Temperature Bounds as a Function of Specific Impulse

IV. CONCLUSIONS

A physics-based power balance model of the NTP TRD engine was assembled in Simulink to examine various cycle configurations and performance specifications. The industry standard Westinghouse correlation for the convective HTC has an uncertainty of $\pm 20\%$.

The current study modified the provided value by the Westinghouse correlation by $\pm 20\%$ to analyze the impacts to the engine performance when the uncertainty limits of the HTC were reached. The datum maximum fuel temperature was 3065.5 K. One of the key findings was that when the HTC was lowered by 20%, the resulting maximum fuel temperature increased to 3192.6 K to by 4.14%. On the other hand, when the HTC was raised by 20%, the maximum fuel temperature dropped to 3010.0 K corresponding to a drop of 1.81%. This suggests that a lower HTC will have a more profound effect on the temperature change which would be detrimental to the engine operation due to a limited operational temperature of the fuel. This work has suggested that experimental studies that will result in lowering the HTC uncertainty are critical for the NTP project as these uncertainties will drive

margins which will affect the predicted engine performance.

This study further analyzed changing the chamber temperature while keeping the chamber pressure and thrust the same to provide an estimation to the engine performance should the HTC yield a higher-than-expected maximum fuel temperature than the datum of the TRD. The results showed that if the chamber temperature and pressure remained constant while the nozzle throat was changed to produce the same amount of thrust, the TRD engine will operate to produce a minimum specific impulse of 715 seconds with modifications to the turbopump and nozzle throat diameter. The reactor parameters remained the same. Furthermore, this study presented a graph of the maximum fuel temperature versus the specific impulse with the $\pm 20\%$ HTC uncertainty values incorporated as the bounding performance cases. This graph can be used to estimate high level vehicle performance approximations given various operating maximum fuel temperature limitations of different fuels for NTP engines.

ACKNOWLEDGMENTS

REFERENCES

[1] Robbins, W. H., and Finger, H. B. *An Historical Perspective of the NERVA Nuclear Rocket Engine Technology Program*. Publication NASA-CR-187154. Analytical Engineering Corporation, 1991.

[2] Gustafson, J., Kreicicki, M., Swanson, R., Zilka, B., and Witter, J. K. Space Nuclear Propulsion Fuel and Moderator Development Plan Conceptual Testing Reference Design. Virtual Event, 2021.

[3] Nikitaev, D., Smith, C., D., and Palomares, K. Nuclear Thermal Propulsion Turbomachinery Modeling. Cleveland, OH, 2022.

[4] Emrich, W. Jr. *Principles of Nuclear Rocket Propulsion*. Butterworth-Heinemann, Kidlington, Oxford, United Kingdom, 2016.

[5] Thomas, G. R. *An Interim Study of Single Phase Heat Transfer Correlations Using Hydrogen*. Publication WANL-TNR--056, 4233809. 1962, p. WANL-TNR--056, 4233809.

[6] Bartz, D. R. "A Simple Equation for Rapid Estimation of Rocket Nozzle Convective Heat Transfer Coefficients." *Journal of Jet Propulsion*, Vol. 27, No. 1, 1957, pp. 49–53. https://doi.org/10.2514/8.12572.

[7] Balje´, O. E. "A Study on Design Criteria and Matching of Turbomachines: Part A—Similarity Relations and Design Criteria of Turbines." *Journal of Engineering for Power*, Vol. 84, No. 1, 1962, pp. 83–102. https://doi.org/10.1115/1.3673386.

[8] Balje´, O. E. "A Study on Design Criteria and Matching of Turbomachines: Part B—Compressor and Pump Performance and Matching of Turbocomponents." *Journal of Engineering for Power*, Vol. 84, No. 1, 1962, pp. 103–114. https://doi.org/10.1115/1.3673350.

[9] Moran, Michael J., Shapiro, Howard N., Boettner, Daisie D., and Bailey, Margaret B. *Fundamentals of Engineering Thermodynamics*. John Wiley & Sons, Inc, 2014.

[10] Bell, I. H., Wronski, J., Quoilin, S., and Lemort, V. "Pure and Psuedo-Pure Fluid Thermophysical Property Evaluation and the Open-Source Thermophysical Property Library CoolProp." *Industrial & Engineering Chemistry Research*, Vol. 53, 2014, pp. 2498–2508. https://doi.org/10.1021/ie4033999.